# Fragmentation and Film Growth in Supersonic Nanoaggregate Aerosol Deposition

Souvik Ghosh<sup>1,3</sup>, Xiaoshuang Chen<sup>1</sup>, Chenxi Li<sup>1,2</sup>, Bernard A. Olson<sup>1</sup>, Christopher J. Hogan Jr. <sup>1\*</sup>

<sup>1</sup>Department of Mechanical Engineering, University of Minnesota, Minneapolis, MN, USA 55455

<sup>2</sup>Current Address: Laboratory for Physical Chemistry, ETH Zürich, 8093 Zürich, Switzerland 
<sup>3</sup>Current Address: Intel Corporation, Hillsboro, OR, USA, 97124

**Submitted to:** 

## **AIChE Journal**

<sup>\*</sup>To whom correspondence should be addressed: hogan108@umn.edu, T: 1-612-626-8312

Abstract

Aerosol deposition (AD) with gas phase-synthesized chain-like nanoaggregates can yield

dense coatings from the impaction of particles on a substrate; however, dense coating formation is

not well understood. Here, we study coating consolidation at the single nanoaggregate level.

Flame spray pyrolysis-made tin oxide nanoaggregates are mobility (size) filtered, accelerated

through a de Laval nozzle, and impacted on alumina substrates. TEM images obtained from low

velocity collection and supersonic deposition are compared via quantitative image analysis, which

reveals that upon supersonic impact nanoaggregates fragment into smaller aggregates. This

suggests that fragmentation is a key step in producing coatings denser than the depositing

nanoaggregates themselves. We supplement experiments with detailed particle trajectory

calculations, which show that the impact energies per atom during nanoaggregate deposition are

below 0.2 eV/molecule. These results suggest that fragmentation can only occur at locations where

nanoaggregates bonded by van der Waals and capillary interactions.

**Topical Heading:** Inorganic Materials: Synthesis and Processing

**Keywords:** Deposition Methods; Particulate Flows; Aerosols; Supersonic Impaction; Aggregates

Introduction

Aerosol deposition (AD)<sup>1-3</sup> is a low temperature, particle-based, additive manufacturing

process which can yield coatings with thicknesses in the 1-100 µm range. It is employed in the

production of ceramic coatings<sup>4-6</sup> with specific dielectic<sup>7,8</sup>, ferroelectric<sup>9</sup>, and thermoelectric<sup>10</sup>

properties, in solar cell production, <sup>11,12</sup> and in the production of tailored surface properties for heat

transfer applications. 13,14 Because of the diversity of materials it can be applied to as well as its

simple implementation, AD will likely find continued application in future manufacturing systems.

2

In AD, micrometer, submicrometer, or nanosized particles are inertially deposited from the gas phase onto a substrate at sub-atmospheric pressures. At deposition particles exceed supersonic speeds (Mach number > 1) and approach hypersonic speeds (Mach number of 5). 15,16 Microparticle AD (also commonly called low pressure cold spray), the most commonly studied form of the technique, typically yields dense coatings, i.e. near bulk density layers formed via plastic deformation of impacting particles. 17-20 Conversely, recent studies 21-24 show that AD techniques utilizing nanoparticles and aggregated nanoparticles (i.e. nanoaggregates, which are more prevalent as nanoparticles typically aggregate during aerosolization<sup>25</sup> or gas phase synthesis<sup>26</sup>) can lead to both relatively dense coatings, exceeding<sup>27,28</sup> the random packing limit of spherical particles, and highly porous coatings.<sup>22</sup> The porosity has been found tunable by modest adjustments to deposition process parameters, including the upstream-to-downstream nozzle pressure ratio and the distance from the nozzle throat to the substrate. Such control over coating microstructure has numerous potential applications, as it provides a means to tune the thermal, optical, and electronic properties of coatings without changing material chemistry or process temperature.

Although tunable, it is presently not possible to design an AD system and set process parameters *a priori* to achieve a desired coating porosity and microstructure. The formation of porous coatings via particle deposition is relatively straightforward to understand and control; both simulations<sup>29-31</sup> and experiments<sup>32-34</sup> focusing on low speed deposition (velocities below 10<sup>2</sup> m s<sup>-1</sup>) reveal that when nanoaggregate deposition occurs without any aggregate deformation or fragmentation, the resulting coating is highly porous and often dendritic. Meanwhile, it is not clear how AD yields coatings which are far denser than the originally synthesized nanoaggregates, and how to set process conditions which yield such dense coatings. The velocity of impacting particles

depends on both their acceleration in the nozzle and their extent of deceleration in the bow shock which typically forms at the substrate surface. Accurate calculations nanoparticle trajectories in such systems have only recently been made possible, as they require knowledge of the particle drag coefficient in a less studied Knudsen number-Mach number regime.<sup>35</sup> There are also limited experimental studies focused on understanding dense coating formation in nanoaggregate AD. The design of inertial impactors for particle collection has shown that at elevated velocities (in excess of 10<sup>2</sup> m s<sup>-1</sup>), nanoaggregates may rebound upon impaction with surfaces or may fragment.<sup>36-38</sup> However, the process conditions and nozzle-substrate geometry for such experiments are typically very different from those utilized in AD (they are typically lower flow rate systems).

In an effort to better understand dense coating formation in nanoaggregate AD, in this study we have experimentally examined changes to nanoaggregate structure resulting from the AD process at the single aggregate level under high speed deposition conditions relevant to coating formation. We generated nanoaggregates of SnO<sub>2</sub> using flame spray pyrolysis.<sup>39</sup> Unique for a study of deposition under conditions relevant to AD, we utilized differential mobility analysis to isolate a fraction of nanoaggregates in a specific mobility window, and then passed nanoaggregates through a de Laval style (converging-diverging) supersonic AD system, where they impacted on a translating Al<sub>2</sub>O<sub>3</sub> substrate. To our knowledge, this is the first investigation of mobility selected nanoaggregate impact in a flow regime relevant to AD, i.e. where nanoaggregate velocities can exceed 300 m s<sup>-1</sup> but the downstream pressure is in excess of 1 Torr (leading to a bow shock), and dense coating formation is demonstrated under the same conditions as experiments as the single nanoaggregate level. Nanoaggregates were similarly collected at lower velocities using an electrostatic sampler. TEM imaging with automated processing, wherein we extrapolate imaged

nanoaggregate structures to three-dimensional quasifractal models, <sup>26,40,41</sup> was then used to quantitatively assess structural changes to nanoaggregates brought about by the AD process. We further coupled our experimental observations with computational fluid dynamics and particle trajectory simulations to predict aggregate impaction velocities under the pressure ratios employed, <sup>35</sup> and to determine the average impact translational energy per atom.

## **Experimental & Numerical Methods**

Flame Spray Pyrolysis

The continuous flow flame spray pyrolysis (FSP) reactor (Figure 1a) utilized to generate SnO<sub>2</sub> nanoaggregates was based on the designs of Pratsinis and coworkers.<sup>39</sup> It was fabricated by ParteQ GMBH (Kuppenheim, Germany). As a precursor solution, Tin(II) Ethylhexanoate (Alfa Aesar) was mixed with 2-Ethylhexanoic acid (Alfa Aesar) at a ratio of 1:3 w/w. Details on FSP system operation to produce SnO<sub>2</sub> nanoaggregates are provided in the supporting information. The FSP reactor was housed within a fume hood enclosure where the air was actively pumped through a HEPA filter and into building exhaust. Figure 1b displays a schematic diagram of the experimental system. A funnel sampler was placed ~ 50 cm above the FSP reactor and was pumped with an Edwards E2M80 rotary pump at ~700 l min<sup>-1</sup>. Such high flow rates served to dilute the aerosol from its particle concentration within the flame, which reduces but does not complete mitigate aggregation during sampling. A  $0.6 - 1.01 \,\mathrm{min^{-1}}$  sample of the aerosol flow was drawn away for analysis and deposition experiments. Sampling was carried out more than ten tube diameters downstream, and with the high Reynolds numbers employed in the sampling system particle concentrations were relatively uniform radially at the point of sampling. This sampled flow was passed through a commercial diffusion drier (TSI Inc. 3062, rated for < 1 1 min<sup>-1</sup> flow rates) to remove excess water vapor, and through a tube furnace (Lindberg blue) at held at 1000°C for residual carbon removal before analysis and deposition. Earlier experiments were performed without the tube furnace, yielding image analysis and mobility analysis results which are not distinguishable from those presented subsequently, hence the furnace only served as a thermal denuder for carbonaceous material and not to sinter or restructure nanoaggregates. Following the diffusion drier the relative humidity at 300 K was below 10% (measured previously for such diffusion driers, though at this humidity water molecules may have remained adsorbed on nanoaggregates), and with the tube furnace with SEM/EDX analysis of nanoaggregates coatings we did not detect any residual carbon. However, this post-flame treatment does not guarantee that all nanoaggregates are composed of primary particles bonded together by sintered bridges. Instead, there was certainly a distribution of particle-particle bond types and bond energies, including sintering bridges, weaker van der Waals interactions, and in instances with residual water, capillary interactions.

## Supersonic Aerosol Deposition

Following the tube furnace, the aerosol flow was passed through a Po-210 radioactive source. In the source sufficient numbers of ion particle collisions led to particles attaining a size and morphology dependent, but relatively material insensitive steady-state charge distribution, <sup>42</sup> at which the majority of particles were uncharged, but there were appreciable numbers of singly charged, doubly charged, and higher charge state particles in the size range examined. After charge conditioning, particles were passed into a differential mobility analyzer (DMA, custom-made, but with identical dimensions to a model 3081 DMA, TSI Inc., Shoreview, MN). The DMA, whose operating principle is discussed in detail previously, <sup>43</sup> only transmits particles within a narrow

mobility (charge to drag ratio) window. DMAs are normally used as "monodisperse" size selection tools (i.e. as bandpass filters). However, because of the existence of multiply charged particles, here DMA selection served simply to filter out nanoaggregates smaller than an effective mobility equivalent size (i.e. it was used a high pass filter that transmits multiply charged larger particles along with singly charged smaller particles of the selected mobility diameter). The DMA was calibrated with 125 nm and 220 nm polystyrene latex particles, and was operated with a recirculating sheath flow of 5.7 l min<sup>-1</sup>. For AD experiments, nanoaggregates were size-selected at applied DMA voltages of 400 V (corresponding to a singly charged mobility diameter of 63 nm), 1000 V (103 nm), and 3000 V (205 nm).

Mobility selected nanoaggregates were then mixed with a clean flow of N<sub>2</sub>, and passed into the supersonic AD system. Depicted in Figure 1c, the AD system consists of a linear gradient slit nozzle with a 2 cm width, an upstream length of 2.54 cm, a downstream length of 3.46 cm, a 0.2 mm thickness at the throat (smaller than most previously utilized AD nozzles), and upstream and downstream contour (half) angles of 4.2% and 1.8°, respectively. Such modest converging and diverging angles are applied to avoid overexpansion of the flow. The nozzle is connected to a chamber where a substrate translation stage is mounted 6.7 mm below the nozzle outlet. The complete assembly is depicted in Figure 1d. The downstream chamber was continuously pumped using a combined Edwards E2M80 vacuum pump and EH200 roots blower system. Pressure taps were inserted both upstream of the nozzle and in the deposition chamber, with the pressure in both regions monitored using a Baratron pressure gage (MKS Instruments).

During deposition experiments, 6 individual 0.76 cm x 1 cm laser machined Al<sub>2</sub>O<sub>3</sub> substrates were mounted in the substrate holder, with a 200-mesh carbon coated copper grids mounted on each substrate to collect particles for transmission electron microscope analysis after

supersonic impaction. The translation stage (automatically controlled) moved at a speed of 1.06 mm s<sup>-1</sup>, corresponding to almost 1 pass per minute, and a single pass was found sufficient for analysis of DMA-selected nanoaggregates. Four separate upstream pressure to downstream pressure ratios were employed in experiments, 101.3 to 1.3 kPa, 66.3 to 0.91 kPa, 25.9 to 0.23 kPa, and 7.9 to 0.07 kPa, respectively. For the highest upstream pressure, 22 l min<sup>-1</sup> of N<sub>2</sub> was mixed with the flow exiting the DMA. For each of the reduced upstream pressure experiments, an orifice (operated in sub-critical conditions in some circumstances) was placed upstream of the nozzle and the dilution N<sub>2</sub> was reduced such that 0.6 – 1.0 l min<sup>-1</sup> of aerosol flow was still pulled through the DMA. With 101.3 to 1.3 kPa upstream to downstream conditions, experiments were carried out with all three DMA set points. At reduced pressures only the 1000 V DMA setting was employed. For all test conditions, we did not observe any nanoaggregate "bounce", i.e. impaction with the surface followed by rebound. Bounce events are detectable in the deposition system as they lead to the formation of visible a porous deposit on the top of the deposition chamber, on the both sides of the nozzle.

In addition to experiments with DMA selection, experiments were performed with the DMA bypassed at the 101.3 to 1.3 kPa pressure ratio condition to examine the formation of coatings. The coatings produced were characterized after 1-25 minutes (1-25 passes) of deposition via scanning electron microscopy (SEM) and X-ray diffraction (XRD), as discussed in the *Electron Microscopy & Material Analysis* subsection.

#### Electrostatic Collection

For each supersonic aerosol deposition experiment with DMA selection, nanoaggregates were also collected on carbon-coated 75-mesh copper grids at low velocities using a TSI Inc.

nanometer aerosol sampler 3089.<sup>44</sup> The TEM grids were mounted with double-sided carbon tape on the sampling plate; the plate was biased at -10 kV with aerosol delivered at flow rate of 1 l min<sup>-1</sup>. Nanoaggregates had an estimated deposition velocity of the order of 10<sup>0</sup> m s<sup>-1</sup> (calculated from the particle electrical mobilities and the field strength applied in the instrument). Mobility based size distribution functions of nanoaggregates were also collected by stepping the DMA voltage in the 50 V- 6500 V range in 10 V increments and detecting particles using a TSI Inc. 3786 condensation particle counter. The resulting mobility based size distribution functions were inverted using a non-linear least squares method.

## Electron Microscopy & Material Analysis

In total, deposition experiments resulted in DMA selected nanoaggregates collected at supersonic velocities and collected electrostatically, as well as coatings produced after 1-25 minutes of deposition (1 to 25 passes as the stage scan rate was approximately 1 one per pass). We imaged DMA selected nanoaggregates after deposition using a Technai T12 transmission electron microscope with an acceleration voltage of 120 kV at the University of Minnesota Characterization Facility. Following previous studies,  $^{26,40,41}$  an in-house MATLAB script was used to identify aggregate projections in images, and to then fit each identified aggregate to a quasifractal (statistical) model by calculating properties of the detected projections. In the quasifractal model, the number of primary particles in an aggregate N, is linked to the aggregate radius of gyration via the equation:

$$N = k_f \left(\frac{R_g}{a_p}\right)^{D_f} \tag{1}$$

where  $D_f$  is the fractal dimension (ranging from 3.0 for compact aggregates to 1.0 for straight chains),  $k_f$  is the pre-exponential factor,  $R_g$  is the three-dimensional radius of gyration, and  $a_p$  is

the primary particle radius. Fitting was performed specifically following the approach described by Chen et al,  $^{26}$  in which the normalized perimeter, longest end-to-end distance, observable projected area, and two-dimensional radius of gyration are calculated for each nanoaggregate projection, and then compared to these four parameters calculated for more than 60,000 projections of computational generated aggregates (using the cluster-cluster algorithm of Filippov et al<sup>45</sup>) of prescribed  $k_f$ ,  $D_f$ , and N (with a maximum of N = 3000). The results of the fitting procedure are the weighted average values of  $k_f$ ,  $D_f$ , and N for each imaged aggregate projection. Prior research has shown that although this approach does not enable precise extrapolation of the three-dimensional architecture of all nanoaggregates, the reconstructed quasifractal aggregates with best fit values of  $k_f$ ,  $D_f$ , and N have drag coefficients and mass-drag (mass-mobility) scalings in good agreement with experimental measurements. For each deposition condition, 160 to 400 individual aggregates were analyzed. As discussed in the *Results & Discussion* section, we utilized the inferred  $k_f$ ,  $D_f$ , and N values for each aggregate to determine to what extent supersonic deposition led to fragmentation and restructuring.

We also imaged deposited coatings using by bisecting the coated substrates and mounting them vertically under a scanning electron microscope (Hitachi S4700). To ensure crystalline SnO<sub>2</sub> synthesis, XRD was performed using a Bruker D8 Discover on both coatings and collected powder (low velocity collection). The resulting spectra were peak fit using the Scherrer equation to infer a mean crystallite size.

## Particle Trajectory Simulations

To estimate the velocities of nanoaggregates upon impact with the substrate to correlate with experimental observations, we simulated both the flow profile in the AD system and particle

trajectories following the approach of Li et al.<sup>35</sup> For flow simulations, we utilized ANSYS Fluent v19 to model the conservation of fluid mass, momentum (via Menter's shear stress transport turbulence model for compressible flow), and energy in the AD system. Details on the number of elements used in calculations and simulation convergence criteria are provided in the supporting information, along with contour plots of the flow velocity, temperature, and pressure under the four examined conditions (Figure S1).

Assuming one-way coupling (a particle dilute system), we modeled particle trajectories in the AD system using a Lagrangian particle tracking approach, accounting for particle inertia and drag. As particles migrate through a nozzle they transition through a highly variable Mach number and Knudsen number regime, for which neither continuum drag models nor low speed (incompressible) drag models are applicable. Prior simulations and measurements<sup>46</sup> do provide a drag coefficient applicable to nanoaggregates across a wide Knudsen number range, but not one applicable to nanoaggregates (non-spherical particles) at elevated Mach numbers. We therefore modeled nanoaggregates as spheres in trajectory calculations, and utilized the drag model provided by Li et al, 35 which is a neural network fit to a compilation of available experimental measurements<sup>47</sup> and direct simulation Monte Carlo results. This model enables computation of the drag coefficient as a function of the local Mach number (particle relative velocity to the local speed of sound ratio) and Knudsen number (gas mean free path to particle diameter). Trajectory calculations were carried out for 10 nm - 600 nm diameter particles seeded uniformly along the nozzle upstream width, with assumed densities of 6950 kg m<sup>-3</sup> (the SnO<sub>2</sub> bulk density), 3500 kg m<sup>-3</sup>, and 1000 kg m<sup>-3</sup>. As nanoaggregates typically behave similar to particles of low density aerodynamically; the choice to model three densities was thus made in an effort to account for varying degrees aggregation. While improved drag laws are certainly needed for exact

calculations of nanoaggregate impaction, variable density simulations nonetheless provide order of magnitude estimates of nanoaggregate impact velocities and kinetic energies to aid in interpreting experimental observations.

#### **Results & Discussion**

Nanoaggregate size distribution & Coating Characterization

Inverted number based mobility diameter distributions  $(dn/dD_p)$ , where n is number concentration and  $D_p$  is mobility diameter) of deposited particles from three separate days of experiments are shown in Figure S2. Though there is day-to-day variability in the concentration of nanoaggregates produced (which is anticipated with FSP), aggregate size distributions were repeatably broad, with peak (mode) mobility diameters near 100 nm. The singly charged DMA set point diameters used in experiments (63 nm, 104 nm, and 205 nm) spanned the high concentration region of the distribution function. XRD spectra of the filter collected powder and of the deposited coatings are shown in Figure S3a, with reference peak locations for SnO<sub>2</sub> labelled. XRD spectra confirmed that FSP generated crystalline SnO<sub>2</sub>, and Scherrer equation analysis (Figure S3b) of the spectra led to an inferred powder crystallite size of 5.66 nm, and a supersonically deposited coating crystalline size of 7.80 nm. Considering how nanoparticles form in FSP, the disparity in mobility diameter and crystallite size suggests that FSP synthesized SnO<sub>2</sub> particles are highly aggregated (with direct evidence provided subsequently). While the detected increase in crystallite size for the supersonically deposited coating may have been caused by the heating of nanoaggregates during high speed deposition, <sup>18,35</sup> this change is small, and as inferred crystallite sizes can be affected by background subtraction procedures, we do not believe this difference suggests AD leads to changes in nanoparticle crystallinity.

Figure 2a-i displays selected SEM cross sectional views of coatings deposited for 1-25 minutes. Figure S4 displays zoomed out SEM images of films after 25 minutes of deposition, demonstrating coating uniformity. The Al<sub>2</sub>O<sub>3</sub> substrate appears darker than the SnO<sub>2</sub> coating in each image. These images show that coatings increase in thickness over time, and that below 5 minutes films are noticeably porous. Relatively dense coatings (on the micrometer scale) result for deposition times of 7 minutes and longer. While efforts to infer the porosity via weighing substrates proved to be too variable (high uncertainty), we can state that at longer times, the porosity drops below 0.50 and is significantly lower than the effective porosities of individual nanoaggregates (which can have effective porosities > 0.90). The deposited film thickness is quantified in the film thickness vs deposition time plot shown in Figure 2j. Each data point represents the average thickness measured through the image analysis of cross-sectional images at multiple different locations of 14 different samples against each deposition condition. From Figure 2j we observe that the initially deposited layer at 1 min is approximately 15 µm thick, and then with longer deposition up to 5 min, surprisingly the thickness decreases to  $< 5 \mu m$ . Following this, with even longer deposition time up to 25 min the film thickness increases monotonically. This suggests that the initially deposited SnO<sub>2</sub> nanoaggregates first undergo densification by further deposition, followed by denser film growth.

Supersonic Aerosol Deposition of DMA selected Nanoaggregates.

In addition to acting as a high pass (in mobility diameter) filter, in this study, the DMA selection serves to dilute the aerosol prior to deposition, enabling examination of nanoaggregates at the single nanoaggregate level. Selected TEM images collected via both electrostatic deposition and supersonic deposition (101.3 to 1.33 kPa, upstream pressure to downstream pressure) are

shown in Figure 3. Electrostatic deposition reveals that as anticipated, FSP leads to the formation of chain-like nanoaggregates composed of  $10^2$ - $10^3$  primary particles (with an average primary particle radius near 7 nm for the SnO<sub>2</sub> aggregates). Also evident is that TEM images of electrostatic deposits had larger nanoaggregates, which appeared to be sparsely populated on grids, while TEM images of supersonic deposits had smaller nanoaggregates, with a higher degree of grid coverage (for the same deposition time and aerosol mass flow rate). While this is partly attributed to the lower collection efficiency of the electrostatic sampler (an imperfect collector) and the supersonic deposition system (a near perfect collector in the absence of bounce), higher grid coverage (by number) is also evidence of nanoaggregate fragmentation. Qualitative comparison of images from the two deposition processes hence suggests that supersonic deposition leads to the fragmentation of nanoaggregates, and that the fragments do not rebound from the surface. This is in-line with prior studies, which revealed that supersonic deposition (though at lower velocities than employed here) did lead to aggregate fragmentation,  $^{36,38}$  and when aggregates fragment, they do not rebound (bounce) from the substrate surface.

SEM and TEM imaging alone therefore confirm the findings of prior work, i.e. AD of nanoaggregates facilitates the formation of dense coatings (as compared to nanoaggregate effective porosities), and nanoaggregates fragment during supersonic deposition. To better quantify the fragmentation process, we inferred the most probable number of primary particles per aggregate, fractal dimension, and pre-exponential factor (N,  $D_f$ , and  $k_f$ , respectively) for nanoaggregates observed in TEM images (as well as a projected area weighted primary particle radius). To demonstrate three-dimensional reconstruction, for selected nanoaggregate images we employed the cluster-cluster algorithm to computationally generate quasifractal aggregates with these inferred properties. A comparison of the images to their 3-dimensional extrapolations is provided

in Figure 4, for both electrostatically and supersonically deposited nanoaggregates and nanoaggregate fragments. Though qualitative, visual comparison of the projections and computationally generated aggregates show consistent structural similarities, hence we elect to utilize the three dimensional properties of computationally generated aggregates to better quantify how supersonic deposition alters nanoaggregate morphology.

Figure 5 displays plots of the inferred number of primary particles per aggregate as a function of the measured two-dimensional radius of gyration for electrostatically and supersonically deposited nanoaggregates (with symbol size scaled non-linearly by inferred aggregate volume,  $V_a = \frac{4\pi N}{3} a_p^3$ ). The disparity between the nanoaggregate fragment sizes is apparent; the supersonically deposited nanoaggregate fragments are clustered in regions of smaller primary particle number and radius of gyration in the plot. There is little to no difference in the fragment sizes between DMA selected mobility diameters of 63 nm and 104 nm, though this may be because a large fraction of the nanoaggregates transmitted at the 63 nm setting were doubly and triply charged (and larger than 63 nm in true drag equivalent diameter). Meanwhile, the nanoaggregate fragments resulting from 205 nm mobility diameter deposition are on average, larger in number of primary particles per aggregate than nanoaggregate fragments from the smaller mobility diameter settings. This implies that larger nanoaggregates may yield larger fragments.

To compare nanoaggregate morphologies, we define a "sphericity"  $\Theta$  for nanoaggregates and nanoaggregate fragments using the equation:

$$\Theta = \frac{V_a - V_c}{V_S - V_c} = \frac{\frac{4\pi N}{3} a_p^3 - V_c}{V_S - V_c} \tag{2}$$

where  $V_a$  is the inferred nanoaggregate volume resulting from quasifractal analysis,  $V_c$  is the volume of a cylinder of radius equal to the nanoaggregate's primary particle radius and length equivalent to the radius of gyration of the nanoaggregate, and  $V_s$  is the volume of a sphere with

same radius of gyration. The sphericity  $(\Theta)$  hence has a maximum value of 1.0 (a perfect sphere) and at sizes larger than the primary particle radius, a minimum of 0.0 (a straight chain). Sphericity values are plotted in Figure 6 for nanoaggregates and supersonically deposited nanoaggregate fragments versus radius of gyration. For each of the three applied DMA settings, focusing first on the electrostatically deposited nanoaggregates, the minimum radius of gyration is near ½ of the DMA set singly charged mobility diameter, confirming the DMA functions as a high pass filter (and not a band pass filter because of multiple charging in the sub-µm range). The sphericity is broadly distributed; however, the vast majority of electrostatically deposited nanoaggregates have Θ values below 0.2 (i.e. they are chain-like). Meanwhile, nanoaggregate fragments are more uniformly distributed in  $\Theta$ , and not only are they smaller in number of primary particles per aggregate, but also many of them are structurally much more compact than the nanoaggregates they are derived from. This is further confirmed in the bottom-right plot of Figure 6, which contains a compilation of all data at 101.3 to 1.33 kPa, as well as the theoretical lines for quasifractal aggregates of variable fractal dimension (noted on each line) and a pre-exponential factor of 1.3. Nearly all of the electrostatically deposited nanoaggregates have  $\Theta$  values falling between the lines for fractal dimensions of 1.8 and 2.6, while a non-negligible number of the supersonically deposited nanoaggregate fragments have  $\Theta$  values above the fractal dimension 2.8 line. We also remark that in all cases there are nanoaggregate fragments with low  $\Theta$  values, indicating that while fragmentation process yields primarily denser fragments, some chain-like structures remain.

Nanoaggregate AD is hence mechanistically different that microparticle AD, <sup>1,5</sup> in that it does not rely on plastic deformation of larger particles which remain intact on deposition and instead hinges upon fragmentation. While the experiments performed do not fully describe why

fragmentation can yield denser coatings, it is noteworthy that with operating conditions which successfully lead to denser coating formation, nanoaggregates clearly fragment into smaller, largely denser (higher sphericity) structures. Two subsequent concerns are then (1) determination of the extent to which changing AD process parameters influences nanoaggregate fragmentation and coating formation, and (2) determination of the reason AD is able to fragment nanoaggregates. To first address (1), sphericity  $\Theta$  is plotted in Figure 7 for supersonically deposited nanoaggregate fragments with four distinct upstream-downstream nozzle pressure settings (and a DMA selected mobility diameter of 103 nm). In all instances, the observed aggregates are smaller than those observed after electrostatic collection, indicating they are nanoaggregate fragments. Despite wide variability  $\Theta$  and the radius of gyration, a clear trend with pressure emerges; deposition at higher pressures results in smaller nanoaggregate fragments. Simulations of particle trajectories help to explain this observation. Figure S5 of the supporting information displays plots of mean particle impaction velocities (averaged over all initial starting locations) as a function of particle diameter (spheres) with three specific densities (with 6950 kg m<sup>-3</sup> being equal to that of bulk SnO<sub>2</sub>). Briefly, results show that for any nozzle, there is an upper size limit (affected by particle density) beyond which particles are not accelerated to the fluid speed. Second, at the substrate surface (for the nozzle design utilized), higher upstream pressures lead to a more intense, higher pressure shock, and smaller particles lack the inertia to migrate though the shock and maintain high speed during impaction. The deceleration of particles is appreciable; all simulated particles  $\leq 100$  nm in diameter decelerate by more than 100 m s<sup>-1</sup> for upstream nozzle pressures of 66.3 kPa and larger. Combining these effects, all impaction speed versus particle diameter plots will display a maximum at a specific particle diameter (the maximum is beyond 600 nm for the higher pressures examined here). The maximum speed particle diameter decreases with decreasing the pressure, but the maximum impaction speed also decreases with pressure. Therefore, in the present study lower pressure deposition reduces nanoaggregate impaction velocity, which we experimentally correlate with a reduced degree of nanoaggregate fragmentation during deposition.

Trajectory simulations additionally provide insight into how nanoaggregates can fragment. We remark that fragmentation could only occur at substrate impact, where complete translational energy to internal energy transfer occurs. While the carrier gas is cold following the nozzle expansion, in the shock region the temperature returns nearly returns to 300 K (see supporting information Figure S1), and while the impact of nanoaggregates may lead to some substrate heating, the extent of substrate heating is certainly not to temperatures sufficient to promote changes to nanoaggregate morphology over time. It is hence the translational energy to internal energy conversion at impact, locally (for nanoaggregates) which drives fragmentation. For a prescribed diameter and effective density, the mean impact velocity can be directly converted into the translational impact energy per particle and per SnO<sub>2</sub> molecule. For an effective density of 1000 kg m<sup>-3</sup>, translational impact energies per particle and translational impact energies per SnO<sub>2</sub> are reported (in electronvolts) in Figure 8a and Figure 8b, respectively. The translational impact energies increase with increasing diameter, under all examined conditions, changing by multiple orders of magnitude. Meanwhile, the translational impact energies per molecule scale with the square of impact velocity only, and are bounded below 0.2 eV per molecule (this is also true with higher assumed densities, and similar to the impact translational energies estimated by Huang et al in supersonic deposition<sup>15</sup>). While the translational kinetic energy per molecule is up to a factor of 5 times the thermal energy at 300 K, it is well below the energy required to break chemical (ionic and covalent) bonds in metal oxides, which are in excess of 1 eV. 49 The assumptions made in trajectory calculations would not change this difference, hence it does not appear that AD is

capable of breaking chemical bonds within SnO<sub>2</sub> nanoaggregates. However, as noted in the "Experimental & Numerical Methods" section, the nanoaggregates synthesized, despite postflame sintering in a tube furnace, likely consist of a wide distribution of bond types and bond energies between primary particles; particles colliding and binding within the flame environment may be connected by sintered bridges (chemical bonds), but those colliding and binding in the post-flame environment (even during sampling) will be held together by a combination of van der Waals interactions, and if residual water remains bound to the tin oxide surfaces, capillary interactions. <sup>50</sup> Salameh et al<sup>34</sup> used molecular dynamics to examine the force displacement curves of TiO<sub>2</sub> aggregates held together by such weaker capillary interactions. Integration of their forcedisplacement curves yields fragmentation and restructuring potential energy barriers near 1 eV, and nanoaggregates composed of up to 10<sup>4</sup> primary particles could certainly have 10<sup>2</sup>-10<sup>3</sup> such bonds. Upon impact and conversion of translational impact energy into internal modes of energy (within the nanoaggregate) there would be ample kinetic energy to drive the fragmentation of nanoaggregates at these non-chemically bound interfaces. This is additionally consistent with the finding of reduced fragmentation at reduced pressure, as in these situations, translational impact energies are reduced (though this is less noticeable on a log scale).

#### **Conclusions**

Nanoaggregate aerosol deposition has been studied in a converging-diverging nozzle system using SnO<sub>2</sub> nanoaggregates generated by flame spray pyrolysis. Dense coating formation was confirmed from SEM images for the operating conditions examined, which also showed the initially the coating thickness does not increase linearly. At the earliest stages of deposition, nanoaggregate impaction leads to porous deposits. This appears to be followed by consolidation

to a denser coating via continued impaction of the nanoaggregates over extended periods of time. To examine this process at the single nanoaggregate level, TEM analysis enabled extrapolation of possible three dimensional architectures for nanoaggregates after both electrostatic and supersonic Such analysis confirmed that nanoaggregates fragment in supersonic aerosol deposition. deposition, and that the fragments released are more closely packed than the initial nanoaggregates. The nanoaggregate AD process is therefore distinct in operation from microparticle aerosol deposition and cold spray deposition, where fragmentation need not occur. Combined experimental characterization and trajectory simulations at variable operating pressure show that the extent of fragmentation is directly linked to the impacting nanoaggregate speeds; higher translational impact energies at deposition are obtained at higher operating pressures, and hence such operating conditions yield smaller fragments. Comparison of the translational kinetic energy per atom to bond energies in metal oxides and binding energies for weakly bound nanoparticles suggests that there is sufficient impact energy for fragmentation of nanoaggregates only at nonchemically bonded interfaces. This is likely the reason why the resulting fragments are still clusters of primary particles (not all bonds are broken). Future studies, informed by the findings noted here, will be needed to examine the consolidation step in nanoaggregate AD and to specifically understand the lower limit achievable in porosity.

## Acknowledgements

Construction of the AD system was supported by ARPA-E IDEAS Program "High-Throughput Discovery of Thermoelectric Materials". S.G. and X.C. acknowledge support from National Science Foundation through the University of Minnesota MRSEC under Award Number DMR-1420013. This contribution was identified by Kuochen Tsai (Shell International E&P) as

the Best Presentation in the session "3D Printing I" of the 2018 AIChE Annual Meeting in Pittsburgh.

#### **Supporting Information**

A list of the symbols utilized, details of fluid flow simulations, nanoaggregate mobility distribution functions, confirmatory evidence of SnO<sub>2</sub> synthesis through X-Ray Diffraction, low magnification SEM images of AD samples, and impaction speed simulation results are provided in the supporting information.

#### References

- Akedo J. Aerosol deposition of ceramic thick films at room temperature: densification mechanism of ceramic layers. *Journal of the American Ceramic Society*. 2006;89:1834-1839.
- 2. Hanft D, Exner J, Schubert M, Stocker T, Fuierer P, Moos R. An overview of the aerosol deposition method: process fundamentals and new trends in materials applications. *Journal of Ceramic Science and Technology*. 2015;6:147-181.
- **3.** Adachi M, Okuyama K, Kousaka Y, Tanaka H. Preparation of gas sensitive film by deposition of ultrafine tin dioxide particles. *Journal of Aerosol Science*. 1988;19:253-263.
- **4.** Adamczyk J, Fuierer P. Compressive stress in nano-crystalline titanium dioxide films by aerosol deposition. *Surface and Coatings Technology*. 2018;350:542-549.
- 5. Akedo J. Room temperature impact consolidation (RTIC) of fine ceramic powder by aerosol deposition method and applications to microdevices. *Journal of Thermal Spray Technology*. 2008;17:181-198.

- **6.** Chun D-M, Ahn S-H. Deposition mechanism of dry sprayed ceramic particles at room temperature using a nano-particle deposition system. *Acta Materialia*. 2011;59:2693-2703.
- 7. Suzuki M, Akedo J. Temperature dependence of dielectric properties of barium titanate ceramic films prepared by aerosol deposition method. *Japanese Journal of Applied Physics*. 2010;49:09MA10.
- 8. Popovici D, Akedo J. Control of powder quality as a method of improving the dielectric properties of (Ba<sub>0.6</sub>,Sr<sub>0.4</sub>)TiO<sub>3</sub> thick films fabricated by aerosol deposition method.

  \*Japanese Journal of Applied Physics. 2010;49:09MA13.
- 9. Suzuki M, Tsuchiya T, Akedo J. Effect of starting powder morphology on film texture for bismuth layer-structured ferroelectrics prepared by aerosol deposition method. *Japanese Journal of Applied Physics*. 2017;56:06GH02.
- 10. Nakamura Y, Matsufuji Y, Inoue M. Fabrication and properties of thermoelectric oxide thick films deposited with aerosol deposition method. *Journal of Physics: Conference Series*. 2012;352:012026.
- 11. Park J-J, Kim D-Y, Lee J-G, Cha Y-H, Swihart MT, Yoon SS. Supersonic aerosol-deposited TiO<sub>2</sub> photoelectrodes for photoelectrochemical solar water splitting. *RSC Advances*. 2014;4:8661-8670.
- Park J-J, Lee J-G, Kim D-Y, Lee J-H, Yun JH, Gwak J, Eo Y-J, Cho A, Swihart MT, Al-Deyab SS, Ahn S, Kim D, Yoon SS. Rapid supersonic spraying of Cu(In,Ga)(S,Se)<sub>2</sub> nanoparticles to fabricate a solar cell with 5.49% conversion efficiency. *Acta Materialia*. 2017;123:44-54.

- 13. Jo HS, Kim M-W, Kim TG, An S, Park H-G, Lee J-G, James SC, Choi J, Yoon SS. Supersonically spray-coated copper meshes as textured surfaces for pool boiling. International Journal of Thermal Sciences. 2018;132:26-33.
- **14.** Jo HS, Lee J-G, An S, Kim TG, James SC, Choi J, Yoon SS. Supersonically sprayed, triangular copper lines for pool boiling enhancement. *International Journal of Heat and Mass Transfer*. 2017;113:210-216.
- Huang C, Nichols WT, O'Brien DT, Becker MF, Kovar D, Keto JW. Supersonic jet deposition of silver nanoparticle aerosols: Correlations of impact conditions and film morphologies. *Journal of Applied Physics*. 2007;101:064902.
- **16.** Fernandez de la Mora J, Hering SV, Rao N, McMurry PH. Hypersonic impaction of ultrafine particles. *Journal of Aerosol Science*. 1990;21:169-187.
- 17. Exner J, Schubert M, Hanft D, Kita J, Moos R. How to treat powders for the room temperature aerosol deposition method to avoid porous, low strength ceramic films.

  \*Journal of the European Ceramic Society. 2019;39:592-600.
- **18.** Lee J-G, Kim D-Y, Kang B, Kim D, Al-Deyab SS, James SC, Yoon SS. Thin film metallization by supersonic spraying of copper and nickel nanoparticles on a silicon substrate. *Computational Materials Science*. 2015;108:114-120.
- 19. Park J-J, Lee J-G, James SC, Al-Deyab SS, Ahn S, Yoon SS. Thin-film metallization of CuInGaSe<sub>2</sub> nanoparticles by supersonic kinetic spraying. *Computational Materials Science*. 2015;101:66-76.
- **20.** Liu T, Leazer JD, Brewer LN. Particle deformation and microstructure evolution during cold spray of individual Al-Cu alloy powder particles. *Acta Materialia*. 2019;168:13-23.

- **21.** Holman ZC, Kortshagen UR. A flexible method for depositing dense nanocrystal thin films: impaction of germanium nanocrystals. *Nanotechnology*. 2010;21:335302.
- **22.** Firth P, Holman ZC. Aerosol impaction-driven assembly system for the production of uniform nanoparticle thin films with independently tunable thickness and porosity. *ACS Applied Nano Materials*. 2018;1:4351-4357.
- 23. Thimsen E, Johnson M, Zhang X, Wagner AJ, Mkhoyan KA, Kortshagen UR, Aydil ES. High electron mobility in thin films formed via supersonic impact deposition of nanocrystals synthesized in nonthermal plasmas. *Nature Communications*. 2014;5:5822.
- 24. Rao NP, Tymiak N, Blum J, Neuman A, Lee HJ, Girshick SL, McMurry PH, Heberlein J. Hypersonic plasma particle deposition of nanostructured silicon and silicon carbide.

  \*Journal of Aerosol Science. 1998;29:707-720.
- 25. Hanft D, Glosse P, Denneler S, Berthold T, Oomen M, Kauffmann-Weiss S, Weis F, Häßler W, Holzapfel B, Moos R. The aerosol deposition method: A modified aerosol generation unit to improve coating quality. *Materials*. 2018;11:1572.
- 26. Chen X, Ghosh S, Buckley DT, Sankaran RM, Hogan CJ. Characterization of the state of nanoparticle aggregation in non-equilibrium plasma synthesis systems. *Journal of Physics D: Applied Physics*. 2018;51:335203.
- 27. McCallister JJH, Keto JW, Becker MF, Kovar D. Influence of normal velocity on microstructure and density of films produced by nanoparticle impact. AIP Advances. 2019;9:035226.
- 28. Chitrakar TV, Keto JW, Becker MF, Kovar D. Particle deposition and deformation from high speed impaction of Ag nanoparticles. *Acta Materialia*. 2017;135:252-262.

- **29.** Lindquist GJ, Pui DYH, Hogan Jr CJ. Porous particulate film deposition in the transition regime. *Journal of Aerosol Science*. 2014;74:42-51.
- 30. Mädler L, Lall AA, Friedlander SK. One-step aerosol synthesis of nanoparticle agglomerate films: simulation of film porosity and thickness. *Nanotechnology*. 2006;17:4783-4795.
- **31.** Baric V, Ciacchi LC, Mädler L. Compaction-induced restructuring of aggregated nanoparticle films using the discrete element method. *Powder Technology*. 2019;342:773-779.
- **32.** Tricoli A, Elmøe TD. Flame spray pyrolysis synthesis and aerosol deposition of nanoparticle films. *AIChE Journal*. 2012;58:3578-3588.
- 33. Castillo JL, Martin S, Rodriguez-Perez D, Higuera FJ, Garcia-Ybarra PL. Nanostructured porous coatings via electrospray atomization and deposition of nanoparticle suspensions.

  \*Journal of Aerosol Science. 2018;125:148-163.
- 34. Salameh S, Schneider J, Laube J, Alessandrini A, Facci P, Seo JW, Ciacchi LC, Mädler L. Adhesion mechanisms of the contact interface of TiO<sub>2</sub> nanoparticles in films and aggregates. *Langmuir*. 2012;28:11457-11464.
- 35. Li C, Singh N, Andrews A, Olson BA, Schwartzentruber TE, Hogan CJ. Mass, momentum, and energy transfer in supersonic aerosol deposition processes. *International Journal of Heat and Mass Transfer*. 2019;129:1161-1171.
- 36. Seipenbusch M, Toneva P, Peukert W, Weber AP. Impact fragmentation of metal nanoparticle agglomerates. *Particle & Particle Systems Characterization*. 2007;24:193-200.

- 37. Ihalainen M, Lind T, Arffman A, Torvela T, Jokiniemi J. Break-Up and bounce of TiO<sub>2</sub> agglomerates by impaction. *Aerosol Science and Technology*. 2014;48:31-41.
- **38.** Post P, Bierwirth M, Weber AP. Mechanical stability measurements of surface modified nanoparticle agglomerates. *Journal of Aerosol Science*. 2018;126:33-46.
- 39. Sahm T, Mädler L, Gurlo A, Barsan N, Pratsinis SE, Weimar U. Flame spray synthesis of tin dioxide nanoparticles for gas sensing. *Sensors and Actuators B: Chemical*. 2004;98:148-153.
- **40.** Jeon S, Hurley KR, Bischof JC, Haynes CL, Hogan CJ. Quantifying intra- and extracellular aggregation of iron oxide nanoparticles and its influence on specific absorption rate. *Nanoscale*. 2016;8:16053-16064.
- **41.** Thajudeen T, Jeon S, Hogan CJ. The mobilities of flame synthesized aggregates/agglomerates in the transition regime. *Journal of Aerosol Science*. 2015;80:45-57.
- **42.** Gopalakrishnan R, Meredith MJ, Larriba-Andaluz C, Hogan CJ. Brownian dynamics determination of the bipolar steady state charge distribution on spheres and non-spheres in the transition regime. *Journal of Aerosol Science*. 2013;63:126-145.
- **43.** Knutson EO, Whitby KT. Aerosol classification by electric mobility: apparatus, theory, and applications. *Journal of Aerosol Science*. 1975;6:443-451.
- **44.** Dixkens J, Fissan H. Development of an electrostatic precipitator for off-line particle analysis. *Aerosol Science and Technology*. 1999;30:438-453.
- **45.** Filippov AV, Zurita M, Rosner DE. Fractal-like aggregates: relation between morphology and physical properties. *J Colloid Interf Sci.* 2000;229:261-273.

- 46. Zhang CL, Thajudeen T, Larriba C, Schwartzentruber TE, Hogan CJ. Determination of the scalar friction factor for nonspherical particles and aggregates across the entire Knudsen number range by direct simulation Monte Carlo (DSMC). Aerosol Science and Technology. 2012;46:1065-1078.
- **47.** Henderson CB. Drag coefficients of spheres in continuum and rarefied flows. *AIAA Journal*. 1976;14:707-708.
- **48.** Gensch M, Weber AP. Rebound behavior of nanoparticle-agglomerates. *Advanced Powder Technology*. 2017;28:1930-1942.
- **49.** Parra RD, Farrell HH. Binding energy of metal oxide nanoparticles. *The Journal of Physical Chemistry C.* 2009;113:4786-4791.
- 50. Laube J, Salameh S, Kappl M, Mädler L, Colombi Ciacchi L. Contact forces between TiO<sub>2</sub> nanoparticles governed by an interplay of adsorbed water layers and roughness. *Langmuir*. 2015;31:11288-11295.

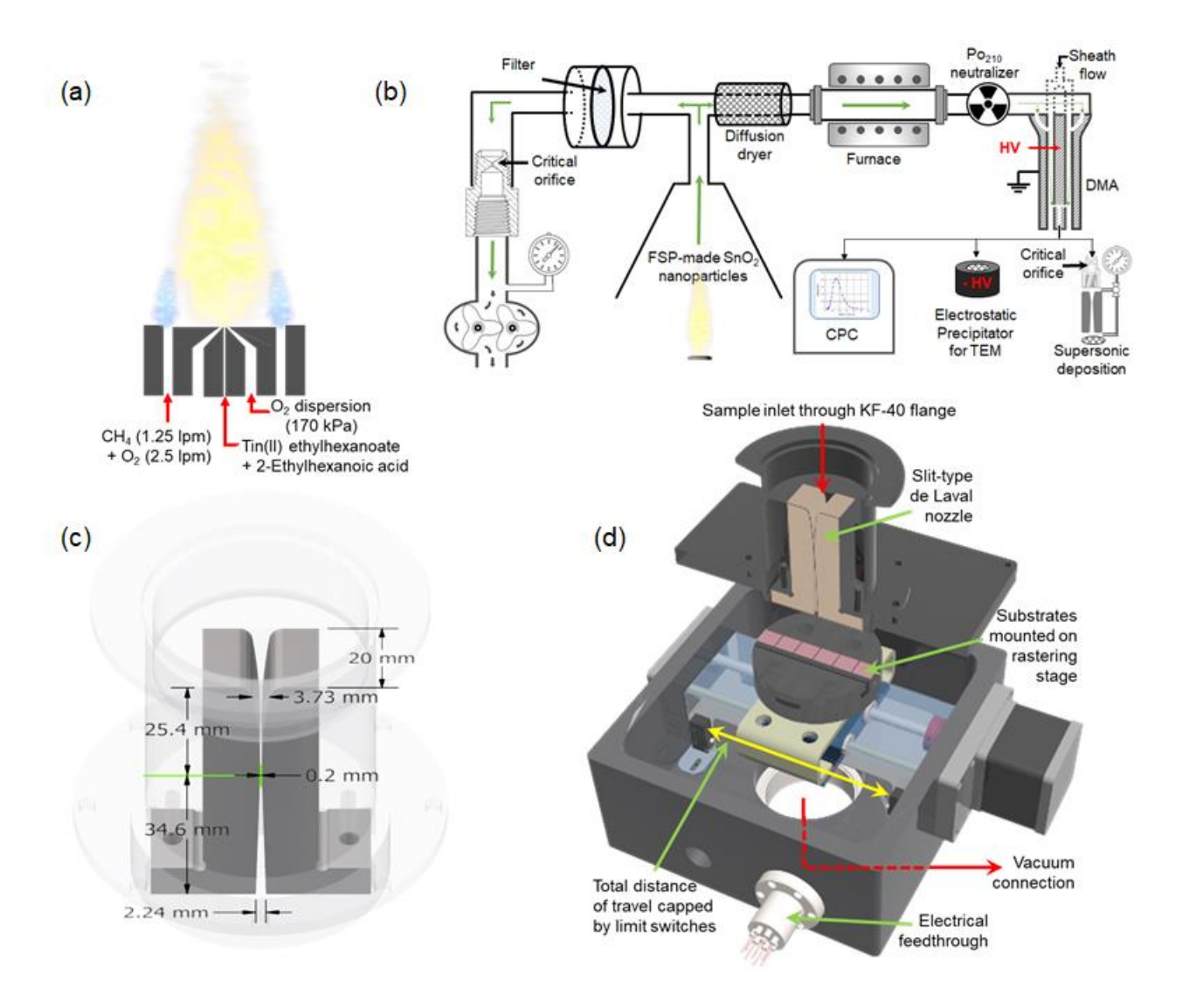


**Figure 1.** Schematic diagrams of (a) the flame spray pyrolysis (FSP) reactor, (b) the combined FSP-differential mobility analyzer (DMA)-supersonic deposition system, (c) the converging-diverging nozzle employed, and (d) the supersonic deposition system, including the translation stage for deposition.

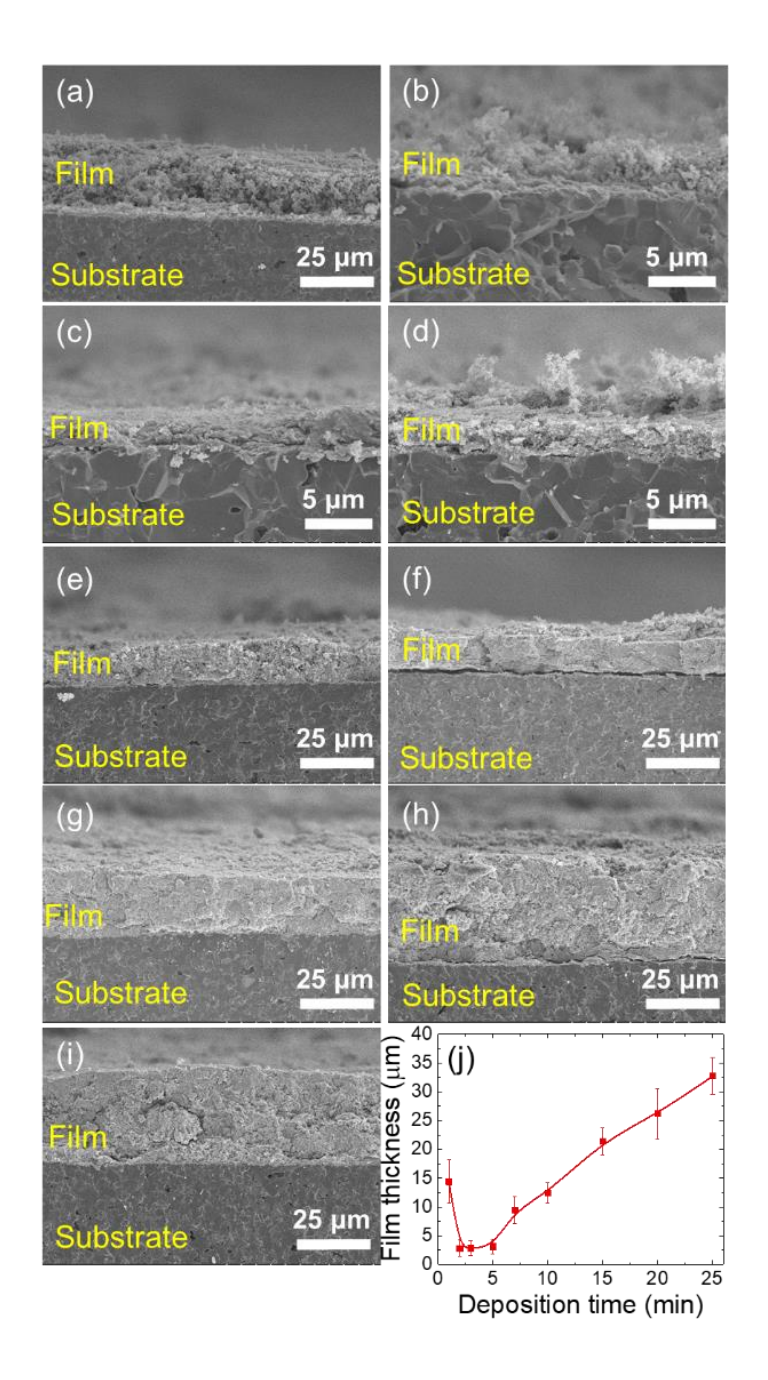


**Figure 2.** Cross sectional SEM images of coatings produced by supersonic deposition of FSP synthesized SnO<sub>2</sub> nanoaggregates with 101.3 kPa upstream, 1.3 kPa downstream nozzle conditions. The coatings were deposited for (a) 1 min, (b) 2 min, (c) 3 min, (d) 5 min, (e) 7 min, (f) 10 min, (g) 15 min, (h) 20 min and (i) 25 min. (j) The supersonically deposited film thickness as a function of deposition time. Error bars represent the standard deviation based on measurements at multiple substrate locations.

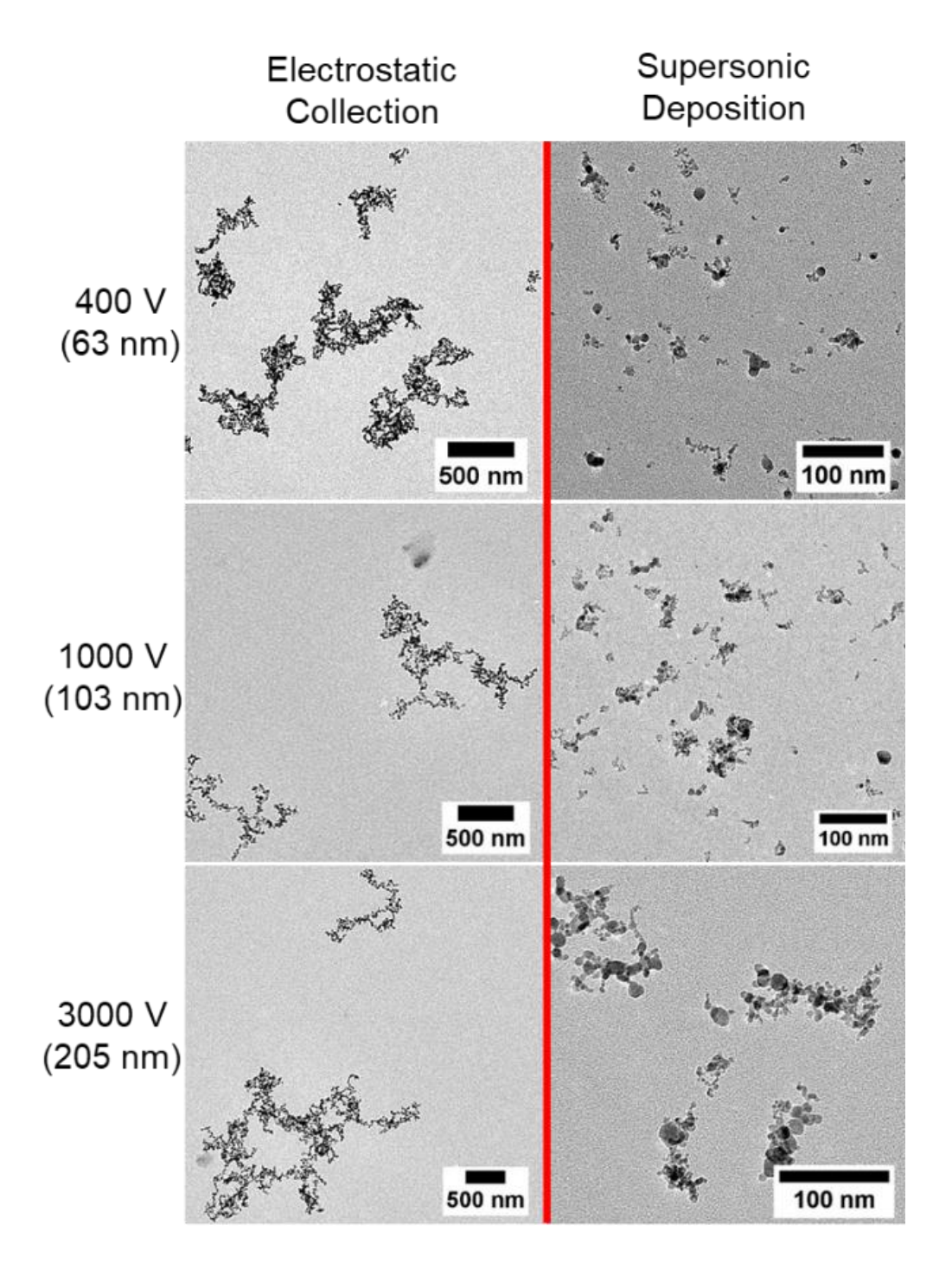


**Figure 3.** TEM images of SnO<sub>2</sub> nanoaggregates and nanoaggregate fragments resulting from electrostatic deposition (left) and supersonic deposition (right) at 101.3 kPa upstream, 1.3 kPa downstream conditions after DMA selection. The applied DMA voltage and nominal singly charged mobility diameter are noted are the respective row values for each column.

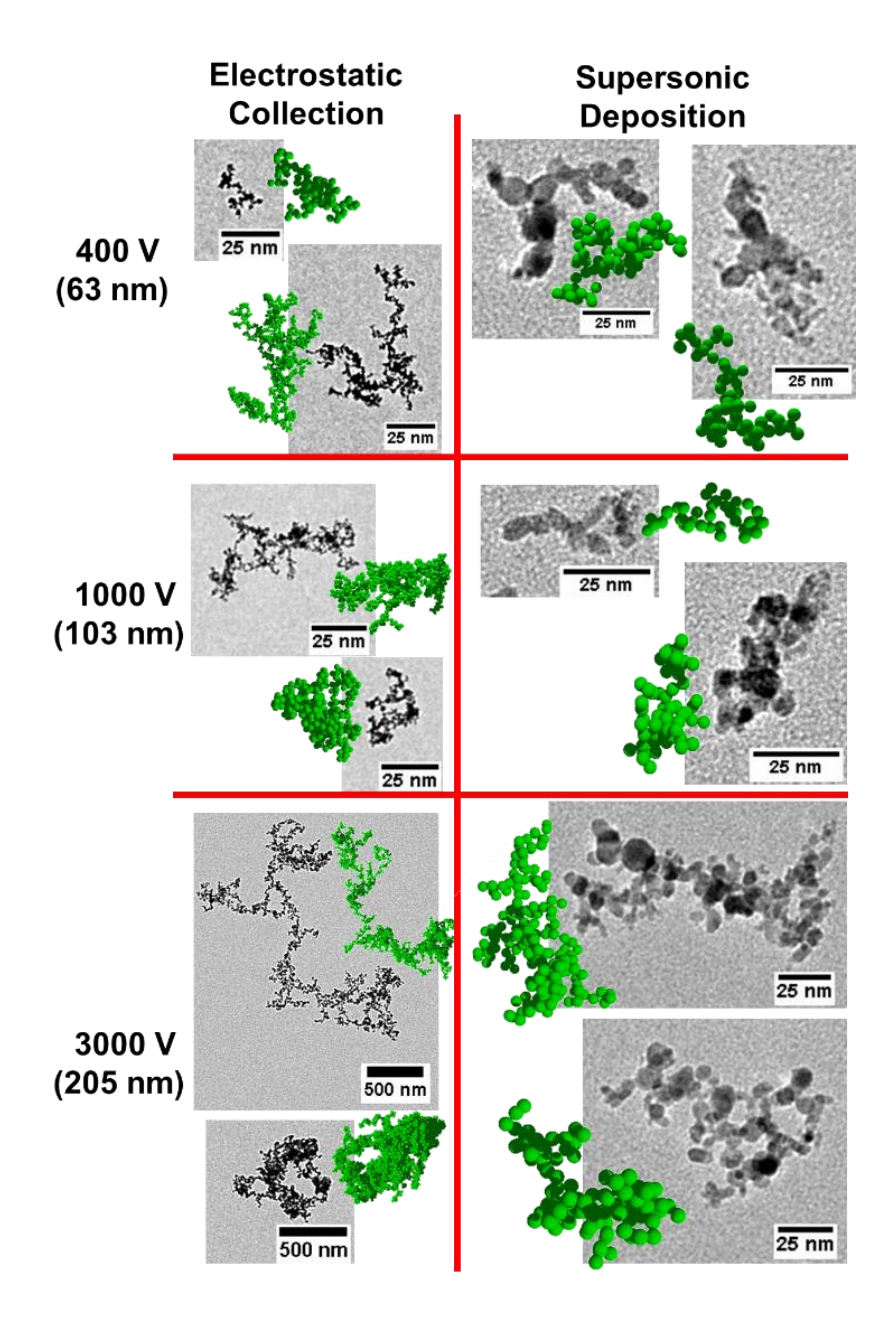


**Figure 4.** Selected TEM images of electrostatically and supersonically (column values respectively) deposited  $SnO_2$  nanoaggregates and nanoaggregate fragments after DMA selection (row values respectively). Shown for comparison are cluster-cluster algorithm reconstructions of quasifractal architectures (green aggregates) with the most probable N,  $k_f$ , and  $D_f$  for each nanoaggregate.

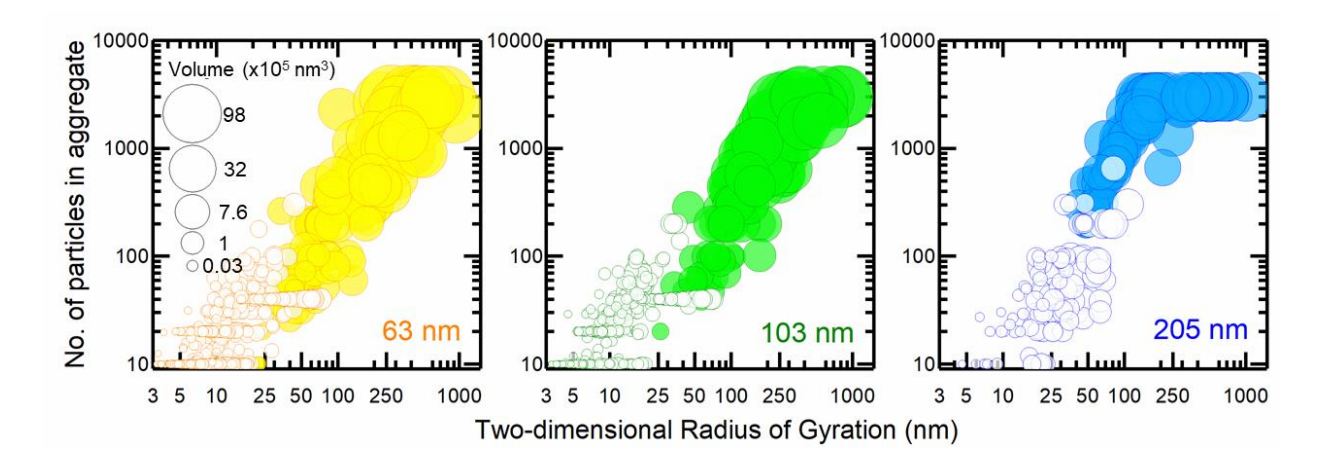


**Figure 5.** The most probable number of particles per aggregate as a function of the measured two-dimensional radius of gyration for each nanoaggregate observed in TEM images, deposited after DMA selection at **(a)** 400 V, **(b)** 1000 V, and **(c)** 3000 V. The singly charged mobility diameter is noted in each plot. Color-filled bubbles represent electrostatically deposited nanoaggregates. Bubbles with no in-fill color represent supersonically deposited nanoaggregate fragments at 101.3 kPa Torr upstream, 1.3 kPa downstream conditions.

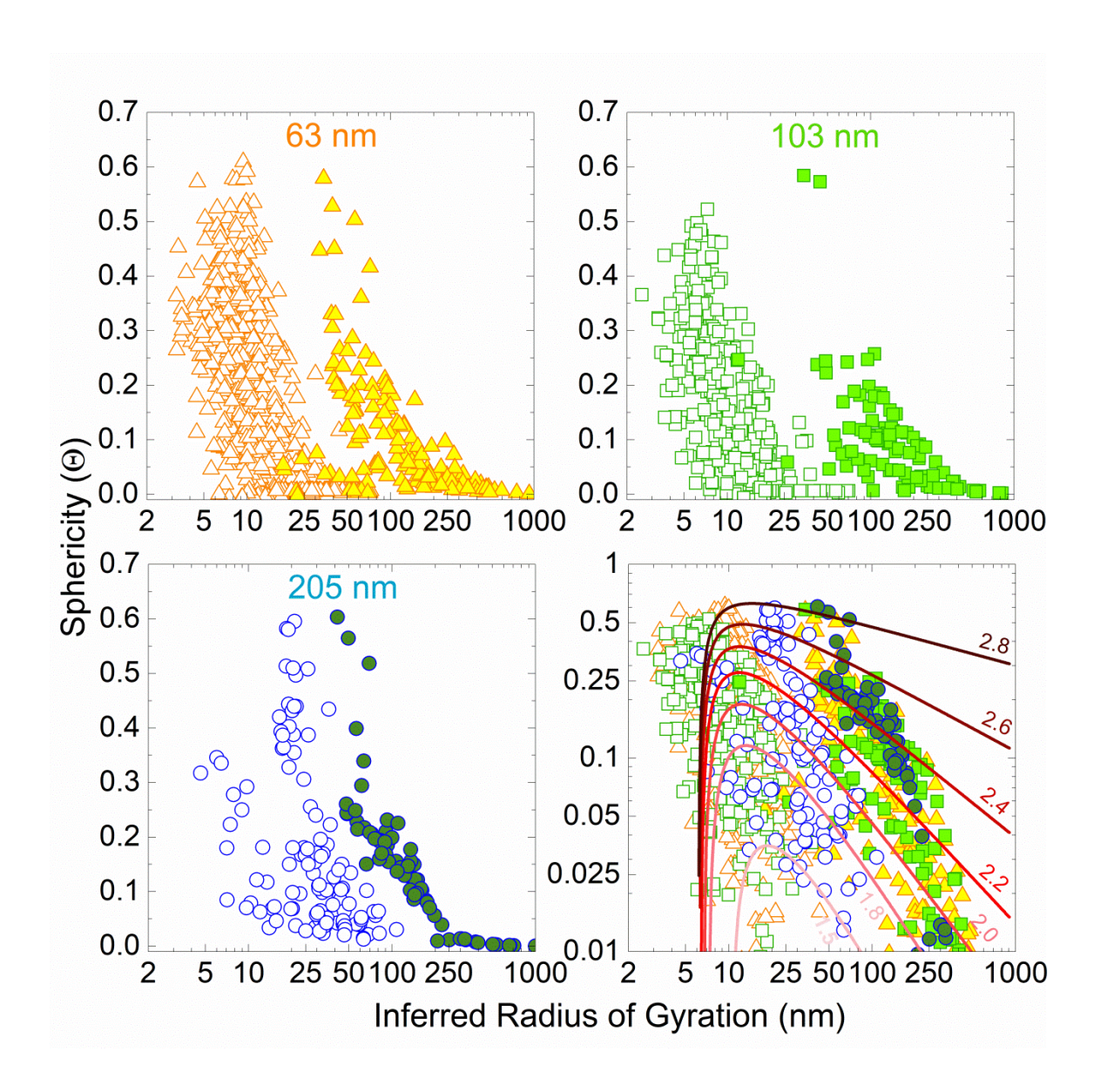


**Figure 6.** The sphericity parameter  $\Theta$ , which spans from 1.0 for spheres to zero for cylinders, as a function of the inferred radius of gyration for all nanoaggregates observed. Symbols with infill color represent electrostatically deposited nanoaggregates. Open symbols represent supersonically deposited nanoaggregate fragments at 101.3 kPa upstream, 1.3 kPa downstream conditions. The summary plot in the bottom right is a cumulative plot of the prior three individual plots of 63 nm, 103 nm and 205 nm nanoaggregates respectively, and is overlaid with the theoretical curves for quasifractal aggregates with the fractal dimension noted.

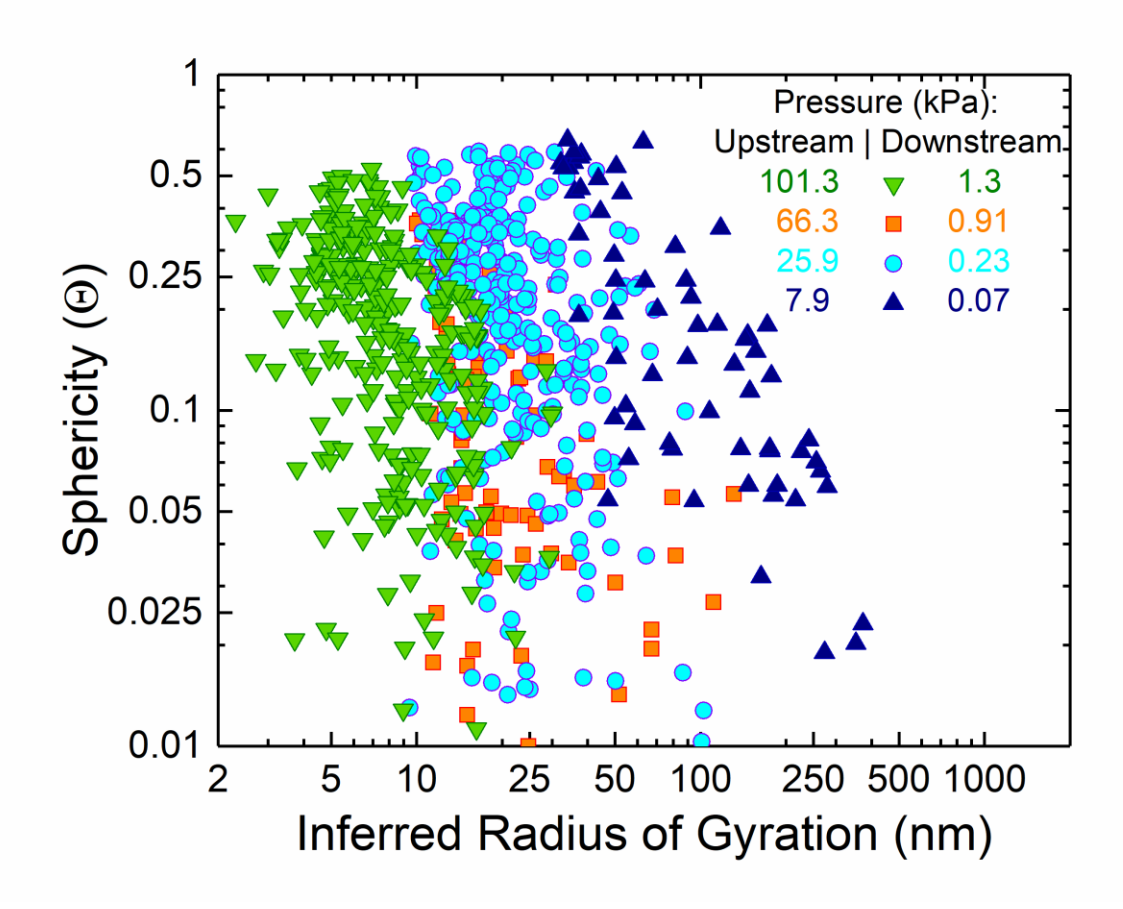


**Figure 7.** The sphericity parameter  $\Theta$  as a function of the inferred radius of gyration for nanoaggregate fragments supersonically deposited at upstream-downstream pressure ratios of 101.3-1.3, 66.3-0.91, 25.9-0.23, and 7.9-0.07 (in kPa). The deposited nanoaggregates were DMA selected at a singly charged mobility diameter of 103 nm.

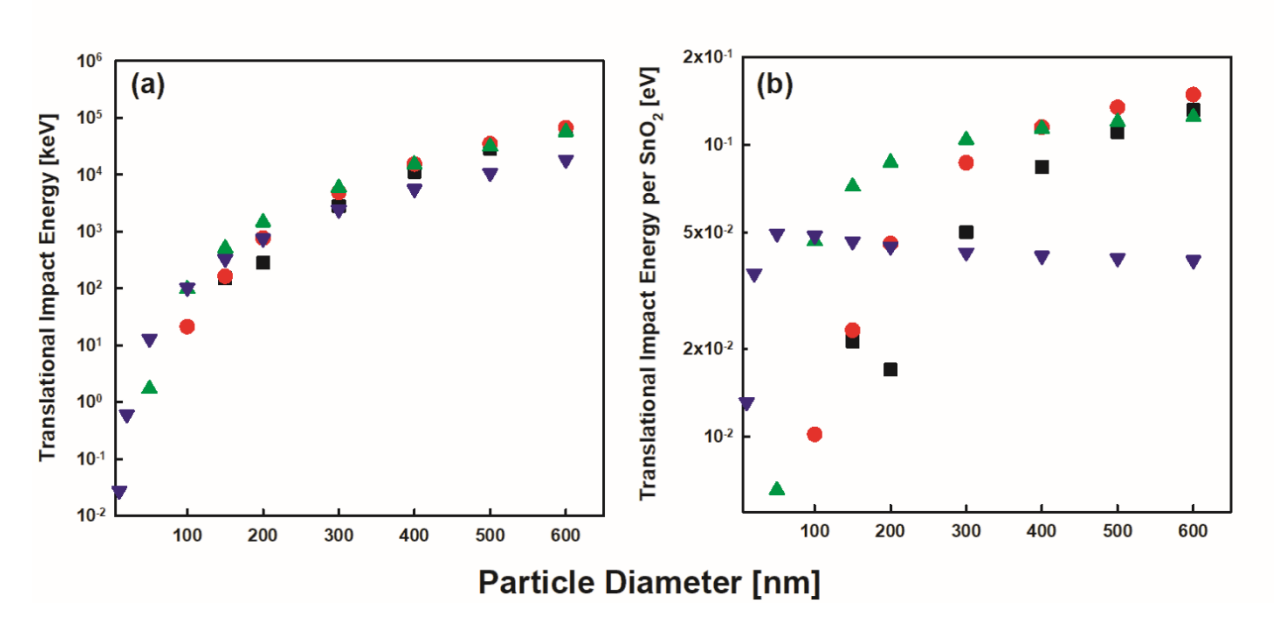


**Figure 8.** The translational impact energy (**a**) and translational impact energy per SnO<sub>2</sub> molecule (**b**) calculated from trajectory calculations assuming an effective nanoaggregate density of 1000 kg m<sup>-3</sup>. Black squares: 101.3 kPa to 1.3 kPa; Red circles: 66.3 kPa to 0.91 kPa; Green triangles: 25.9 kPa to 0.23 kPa; Blue triangles: 7.9 kPa to 0.07 kPa, upstream to downstream pressures.